SATELLITE THERMAL REMOTE SENSING OF THE VOLCANOES OF ALASKA AND KAMCHATKA DURING 1994 – 1996 AND THE 1994 ERUPTION OF KLIUCHEVSKOI VOLCANO

By

William Christopher Wyatt

RECOMMENDED:

Advisory Committee Chair

Department Head

APPROVED:

Dean, College of Science, Engineering and Mathematics

Dean of the Graduate School

12-18-00

Date

SATELLITE THERMAL REMOTE SENSING OF THE VOLCANOES OF ALASKA AND KAMCHATKA DURING 1994-1996, AND THE 1994 ERUPTION OF KLIUCHEVSKOI VOLCANO

A

THESIS

Presented to the Faculty

of the University of Alaska Fairbanks

in Partial Fulfillment of the Requirements

for the Degree of

MASTER OF SCIENCE

By

W. Christopher Wyatt, B.S.

Fairbanks, Alaska

May 2001

Abstract

The Advanced Very High Resolution Radiometers on the NOAA polar orbiting satellites were used to routinely observe the volcanoes of Alaska and Kamchatka from May 1994 to July 1996, as part of the monitoring effort of the Alaska Volcano Observatory. The largest eruption observed during this period occurred at Kliuchevskoi Volcano between September 8 and October 2, 1994. Radiative temperature measurements made during this eruption were used to develop quantitative methods for analyzing volcanic thermal anomalies. Several parameters, including maximum temperature, anomalous pixels, and total volcanic signal (TVS), were compared to viewing angle and date. A new quantity, TVS7, may most effectively monitor the temporal evolution of the eruption using thermal data. By combining several observations of the thermal state of the volcano, the general nature of the volcanic activity can be described. These observations may indicate an elevation in temperature twelve to 24 hours before an ash-producing event.

Table of Contents

List of Figures

List of Tables

Acknowledgements

This research was supported by the United States Geological Survey as part of the Volcano Hazards and Geothermal Studies Program through the Alaska Volcano Observatory, and by additional funds from the State of Alaska and the University of Alaska Geophysical Institute.

I thank the UAF Department of Geology and Geophysics for three semesters of teaching assistantships, and the Geophysical Institute for two years of support as a research assistant. Thanks also to Ken Dean for encouragement and inspiration throughout my tenure as a graduate student, and to my committee members John Eichelberger, Chris Nye, and Game McGimsey for their input into my education.

I thank J.K. for an excellent adventure on Mt. St. Augustine; D.R., A.H., and M.W. for hot times at Pu'u O'o; and J.E. and G.M. for an eye-opening visit to Crater Peak and Ptarmigan Ridge. G.W. gave me the chance to see Erebus on Christmas '99. D.B. revealed the GKS, the Zoroaster, and the Red Lady Ale. B.S., T.L., and S.H. were fine geologists to work with at UNCW. M.F. introduced me to volcanology at SP Mountain in 1990. Otto'Man took the lead on 1000 miles of Alaska trails, keeping me smiling and healthy if not studying.

And muchas gracias to Alina Shale—from the Sagebrush to 65N and back again, you are my four-season bomb-proof shelter, the envy of all on the mountain, and I could not have done this without you.

Chapter 1: Introduction

1.1 Geologic Setting

The volcanoes that were monitored within the scope of this project were created by the subduction of the northern edge of the Pacific plate. The Kamchatkan volcanoes rise above the margin between the Pacific plate and the North American plate on a peninsula approximately equivalent in size to California (figure 1). Nineteen of these have erupted during historical times (Simkin et al., 1994). The volcanoes of the Aleutian Islands, the Alaska Peninsula, and the Wrangell mountains are the result of the collision of the Pacific plate and the North American plate. There are 41 historically active volcanoes in the Aleutian arc (Miller et al., 1998). These span nearly 2500 km from Mount Spurr in the east to Kiska Volcano in the west. To the east, there have been no historical magmatic eruptions in the shield volcanoes of the Wrangells, though there are reports of phreatic explosions at Mount Wrangell in 1819, 1884, and 1902 (Wood and Kienle, 1990; Richter et al., 1995). Throughout the region there are reports of elevated volcanic activity about once each month, with larger eruptions occurring approximately once each year.

1.2 Purpose

1.2.1 Mitigation of Volcanic Hazard to Aircraft

Explosive volcanic eruptions can produce large volumes of finely broken rock fragments (ash), which can rise to altitudes of 30,000 m or more (Casadevall and

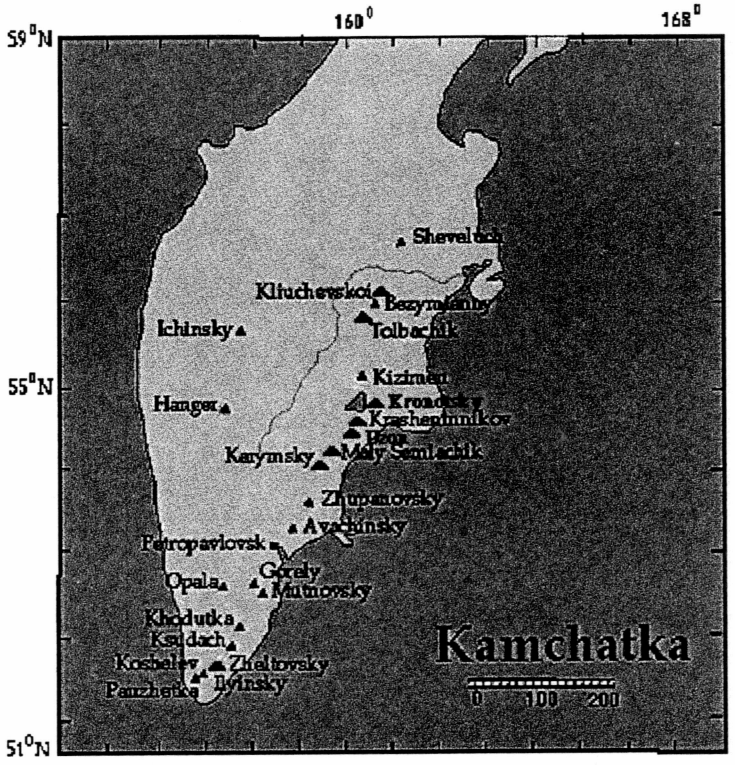

Figure 1. Location map of Kamchatkan volcanoes.

(From Waara et al., 1996).

Thompson, 1995). These ash clouds can remain airborne for several days and commonly drift for thousands of kilometers, affecting areas at great distances from the source volcano. Because the population density in the area of this study is low, the far-reaching effects of volcanic eruption clouds are among the greatest hazards posed by eruptions in Kamchatka and Alaska.

The North Pacific air routes are among the busiest in the world, as flights between North America and Asia follow the great circle path linking international destinations. More than 10,000 passengers and tens of millions of dollars in cargo fly through the region each day (Neal et al., 1997). Airborne volcanic ash poses a particular hazard to aircraft in this region because of the juxtaposition of over 100 active volcanoes and heavily used air routes. Aircraft that encounter volcanic ash can suffer abrasion damage to leading surfaces, cabin air contamination, and engine failure (USGS, 2000).

Established in 1988 to address these and other concerns, the Alaska Volcano Observatory (AVO) has three primary objectives:

1. To conduct monitoring and other scientific investigations in order to assess the nature, timing, and likelihood of volcanic activity;
2. To assess volcanic hazards associated with anticipated activity, including kinds of events, their effects, and areas at risk; and
3. To provide timely and accurate information on volcanic hazards, and warnings of impending dangerous activity, to local, state, and federal officials and the public. (AVO 2000)

In cooperation with the Kamchatka Volcano Emergency Response Team (KVERT), the monitoring effort includes the volcanoes of Kamchata as well. Beginning with the

eruption of Redoubt Volcano in 1989, weather satellites have been used by AVO to monitor the movement of volcanic ash clouds. This study shows that these satellites are also valuable for assessing general thermal conditions at a volcano prior to an ash-producing phase of an eruption. Moreover, by identifying volcanoes that evolve from relative quiescence to unrest, before immediate hazards are created, more diligent monitoring efforts can be initiated at sites that are not routinely monitored by other methods.

1.2.2 Scientific Investigation

The ongoing collection of satellite data at these remote volcanoes is accumulating a vast amount of information that now spans more than a decade. While the spatial resolution of the data used in these efforts is coarse compared to other sources of remotely sensed data and does not allow visual recognition of many kinds of volcanic activity, the value lies in the reliability of the NOAA weather satellite system to provide frequent, inexpensive measurements anywhere within the satellite coverage area. Models of thermal energy flux can be developed from these data, and large scale geomorphic processes can be observed. The thermal state of the exterior of a volcano is a product of processes that occur in the subsurface, and can be incorporated into hypotheses regarding them.

Chapter 2: Background

2.1 Sensor Description

2.1.1 NOAA Polar Orbiting Satellites

The Advanced Very High Resolution Radiometer (AVHRR) sensor is carried aboard the National Oceanographic and Atmospheric Administration (NOAA) TIROS-N series of polar orbiting satellites. The first of this series was launched in 1978 (Kidwell 1991). The primary mission of these sensors is to provide information for weather prediction and monitoring (Lillesand and Kiefer, 1994). The frequent coverage of large areas offered by weather satellites has additionally made them useful for environmental monitoring, natural resource assessment, and other applications as well (Lillesand and Kiefer, 1994). During the period of this study, the satellites NOAA-10, -11, -12, and -14 were used; NOAA-11 failed during this study in September 1994. A useful history of weather satellites can be found in Hastings and Emery (1992).

Each NOAA polar orbiter completes one orbit every 102 minutes, or slightly more than 14 orbits per day, at an altitude of approximately 830 km. Sensors include the AVHRR imaging system and the TIROS Operational Vertical Sounder (TOVS), a cluster of three instruments that measure radiance at different wavelengths associated with particular atmospheric components at different levels of the atmosphere (Kidwell 1991). The mass of the spacecraft is over 1200 kg (Hastings and Emery 1992).

2.1.2 The Advanced Very High Resolution Radiometer

The project described herein uses data from the AVHRR sensor. The sensor has a swath width of approximately 2400 km (figure 2). The scan angle of the sensor ranges from 0° at nadir to 55° at the edge of the swath (figure 3). With an instantaneous field of view of 1.39 mrad, the ground sample distance (GSD) varies as a function of the viewing angle. Raw image data picture elements (pixels) consequently range in size from approximately 1.1 km by 1.1 km at nadir to 2.3 km along track by 5.5 km across track at the far swath edge (Mouginis-Mark et al., 1994).

These data are available in four formats. High Resolution Picture Transmission (HRPT) format is 1.1 km resolution data received in real-time by ground stations including the one at the Geophysical Institute, University of Alaska Fairbanks (UAFGI), and is the format used in this project. Local Area Coverage (LAC) is 1.1-km data custom scheduled for acquisition and recorded on board for later transmission to NOAA ground stations. Global Area Coverage (GAC) data are resampled to create 4.4-km pixels and are also stored for replay. Automatic Picture Transmission (APT) is a lower resolution analog form of HRPT used by low-cost VHF ground stations (Hastings and Emery 1992).

The AVHRR collects data in five wavelength bands. These bands, or channels, are chosen in regions of the electromagnetic spectrum where atmospheric absorption of solar radiation is minimal (figure 4). The primary absorption components of the atmosphere are water vapor, ozone, and carbon dioxide (Rao et al., 1990). Band 1 is in the visible region of the spectrum from 0.58-0.68 μm. Band 2 lies in the near infrared

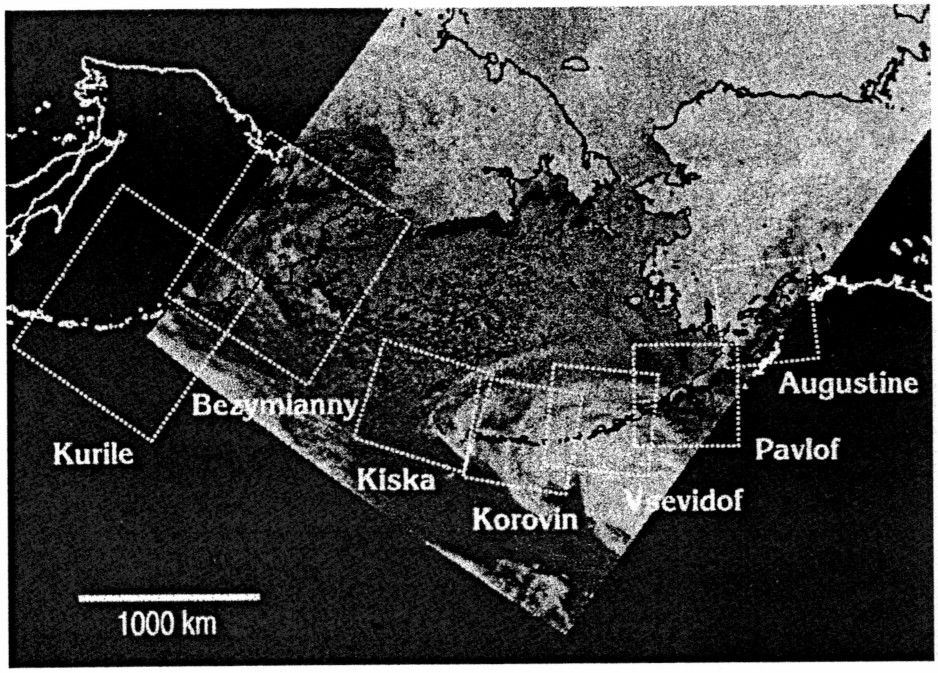

Figure 2. AVHRR swath and volcano monitoring subregions. (From Dean et al., 1998.)

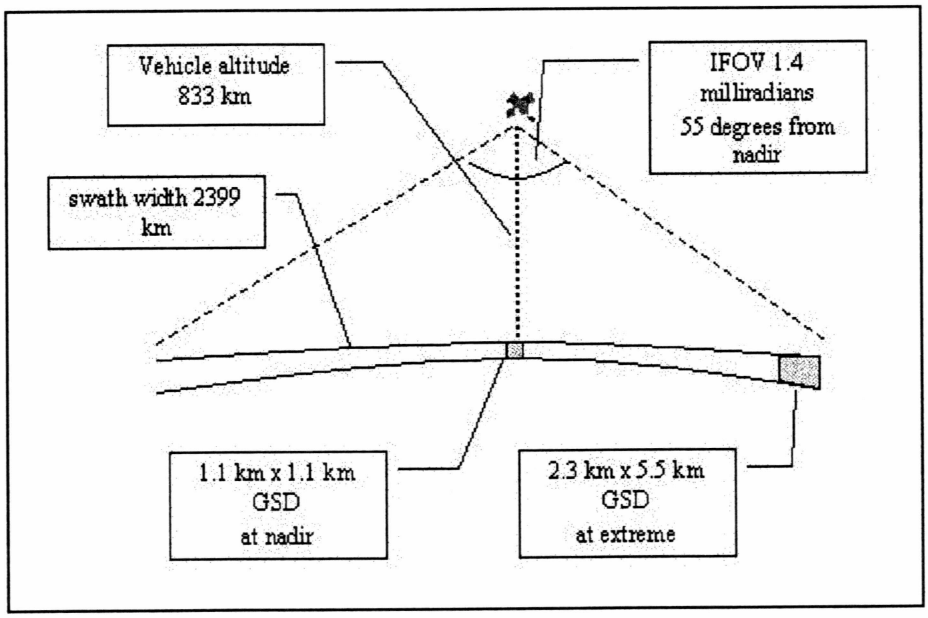

Figure 3. AVHRR viewing geometry.

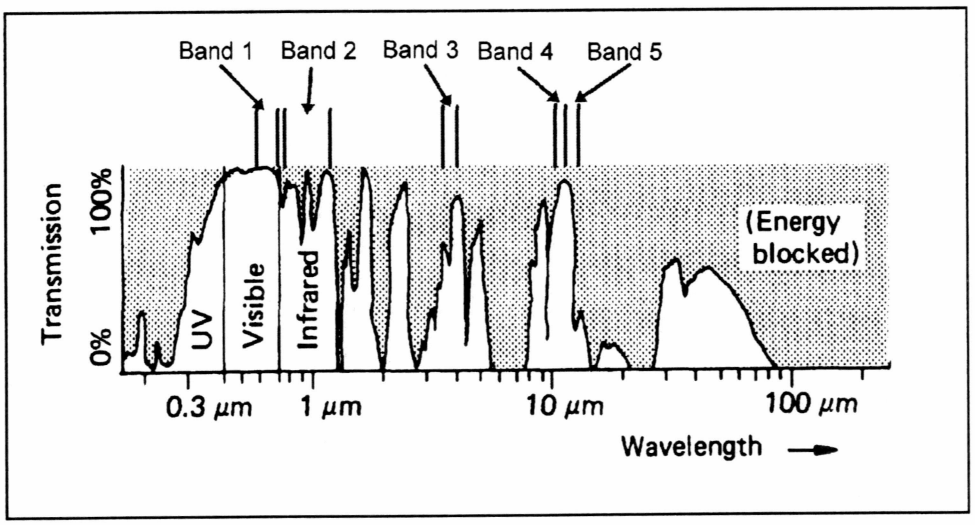

Figure 4. Electromagnetic spectrum, atmospheric absorption, and location of AVHRR bands. (Modified from Lillesand and Kiefer, 1994.)

(IR) region from 0.725-1.1 μm. The values derived from band 1 and band 2 measure reflected solar energy which can be converted into albedo, the ratio of incident radiation (in those wavelengths) to that reflected by clouds or the surface of the earth.

The remaining channels, 3, 4, and 5 are in the thermal IR portion of the spectrum at 3.55-3.93, 10.30-11.30, and 11.50-12.50 μm, respectively. The early AVHRR instruments on NOAA-6, -8, and -10 had only 4 channels, with band 4 at 10.50-11.50 μm; to maintain consistent 5 channel data format, data from these sensors are reported with band 5 as a repeat of band 4 (Kidwell 1991).

2.1.3 The AVHRR Receiving Station

The AVHRR receiving station at the UAFGI receives downlinks from more than 20 satellite passes every 24 hours (Dean et al., 1998). The high latitude of Alaska is advantageous when using AVHRR for monitoring volcanoes. As consecutive orbits of the spacecraft converge at the poles, the swaths begin to overlap. This geometry allows more frequent coverage of a high latitude volcano than of an equatorial volcano of the same longitude. Data is archived at the station on 8-mm tape, and browse imagery is available on the World Wide Web.

The coverage area, or station mask, of the AVHRR receiving station at the UAFGI is approximately a circle of radius 2800-km centered on Fairbanks (figure 5). The satellite transmits data through line of sight radio communication with the Fairbanks ground station, which limits the station mask to areas beneath the satellite when it is above the horizon as seen from the ground station. As the satellite moves along its orbit,

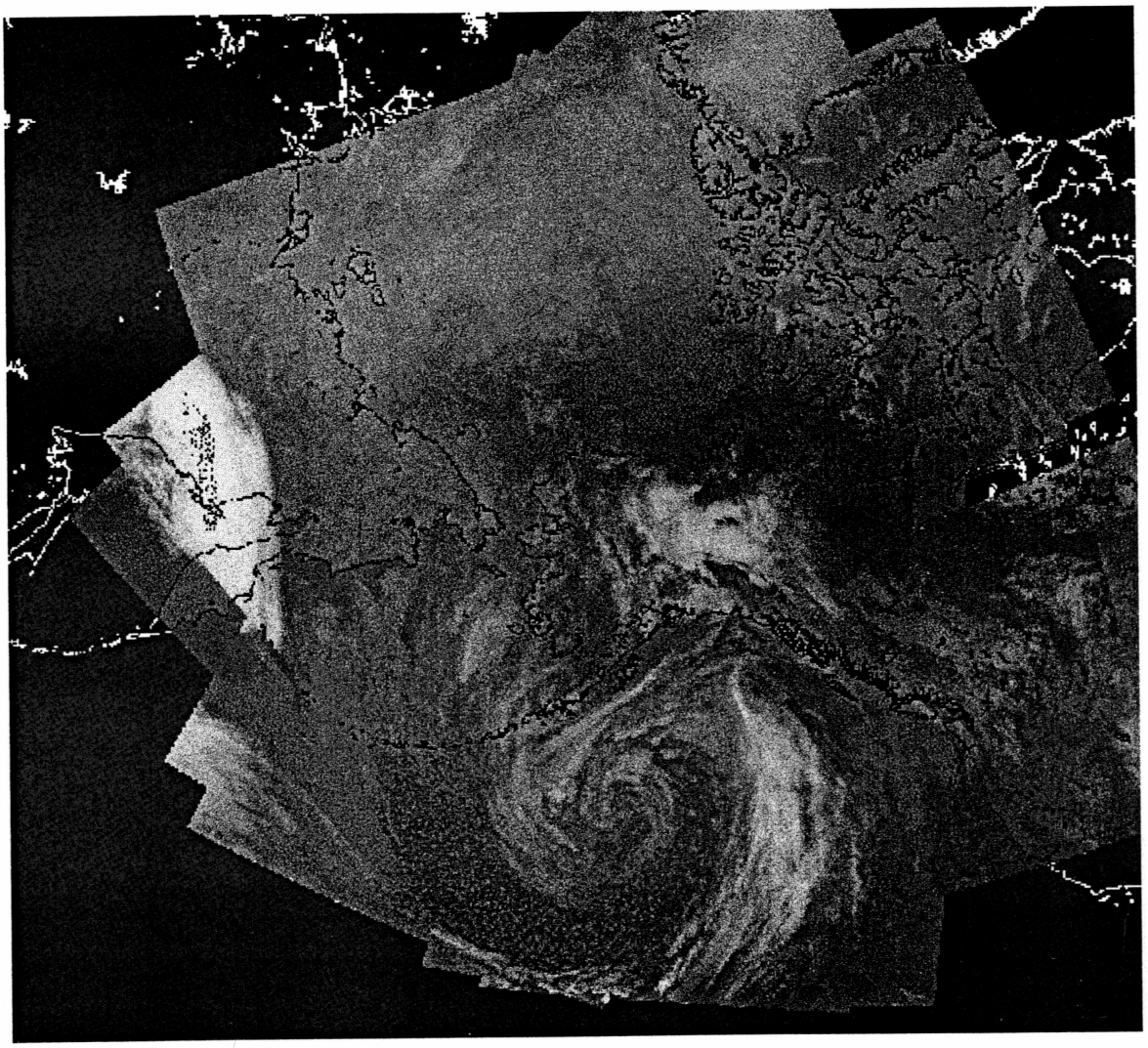

Figure 5. UAFGI AVHRR receiving station coverage area. Overlapping swaths illustrate the size of the station mask, centered on Fairbanks, Alaska.

coverage ends when the satellite disappears below the horizon. Within the mask, areas closer to the Fairbanks ground station are imaged 6-8 times every 24 hours due to the convergent overlapping swaths of consecutive passes in the polar orbit configuration, compared to four times daily over equatorial regions. Coverage frequency decreases with distance from the station. For this reason, more data from the Cook Inlet volcanoes is available than from the volcanoes of southern Kamchatka to the west or the Cascades to the east.

2.1.4 The AVHRR Radiation Detectors

Each of the five bands on the AVHRR uses a photoconductive solid state detector, which converts the incident radiant energy into a measurable quantity (Rao et al., 1990). In bands 1 and 2 the detector element is made of silicon (Rao et al., 1990). Band 3 uses an indium antimonide detector, and those used in band 4 and 5 are made of mercury cadmium telluride (Rao et al., 1990).

Incoming photons produce a change in the electrical conductivity in the detector element, which is connected in series with a load resistor and a battery. The voltage is measured across the load resistor, and the effect of the incident energy is known (Hudson, 1968).

Kidwell (1991) describes the calibration of the AVHRR thermal bands. The input data values (sensor counts) from the detector are converted to energy E, in units of milliwatts/m^2-steradians-cm^{-1}. The energy value is converted to brightness temperature using the inverse of Planck's radiation equation:

$$T(E) = C_2\upsilon/\{\ln(1+C_1\upsilon^3/E)\}$$

where T is the temperature in °K, υ is the central wave number of the band in cm^{-1}, and C_1 and C_2 are constants: $C_1 = 1.1910659 \times 10^{-5}$ milliwatts/m^2-steradians-cm^{-4} and $C_2 = 1.438833$ cm-°K (Kidwell 1991). This value for the surface temperature is the pixel integrated temperature, an average value incorporating the different components at their respective temperatures into one value for the entire pixel.

2.2 Data Processing

The image data used in this study was processed using the SeaSpace TeraScan system in the Alaska Data Visualization and Analysis Laboratory (ADVAL) at the UAFGI. All data were calibrated using the TeraScan 'avcal' utility. The resampled imagery data was resampled using 'fastreg' to 1.1-km pixels and the cubic convolution method and fitted to an Albers equidistant projection. Pixel values were extracted from 7 by 7 kilometer grids centered at the volcano summit and imported into Microsoft Excel for analysis.

2.3 Monitoring Regions

At the Alaska Volcano Observatory, data from the north Pacific Ocean region is divided into seven sectors to create a manageable and efficient system for AVHRR monitoring of all the volcanoes (figure 2). These sectors are named after a volcano near the center, and include Augustine, Pavlof, Vsevidof, Korovin, Kiska, Bezymianny, and Kurile. Each square region in the Alaskan portion is 563 km on a side (512 pixels), and

those covering Kamchatka and the Kuriles are 1126 km on a side (1024 pixels). The five sectors encompassing the Alaskan volcanoes overlap enough to ensure complete coverage. The area between the Kiska sector and Bezymianny sector, including the Kommandorski Islands, has no active volcanoes. For the purpose of monitoring drifting eruption clouds, large sectors covering the Bering Sea and the Gulf of Alaska are established as well.

2.4 Satellite Monitoring Routine

Since the completion of the data collection period of this study, many advances have been made in the satellite data monitoring of volcanoes at AVO. Automated subscene extraction, anomaly identification, and personnel notification are among these improvements (Dean et al., 1998).

All five AVHRR bands are used during routine monitoring to highlight different features in the images, including topography, thermal structure, meteorological and eruption clouds, and shorelines. The five bands are discussed below in the order of their use by AVO analysts with a typical image example selected for monitoring.

The band 3 image is examined first to reveal any high temperature thermal anomalies or eruption clouds. Because band 3 (3.53-3.93 μm) is near the peak wavelength of thermal radiation emitted by a body at the temperature of lava (on the order of 1000 ˚C or 1273 ˚K), it is the AVHRR channel most sensitive to hot features on the ground (figure 6). Harris et al. (1995) showed that an area of lava as small as 100 m^2 can saturate a band 3 pixel, reaching or exceeding the maximum value at which it can

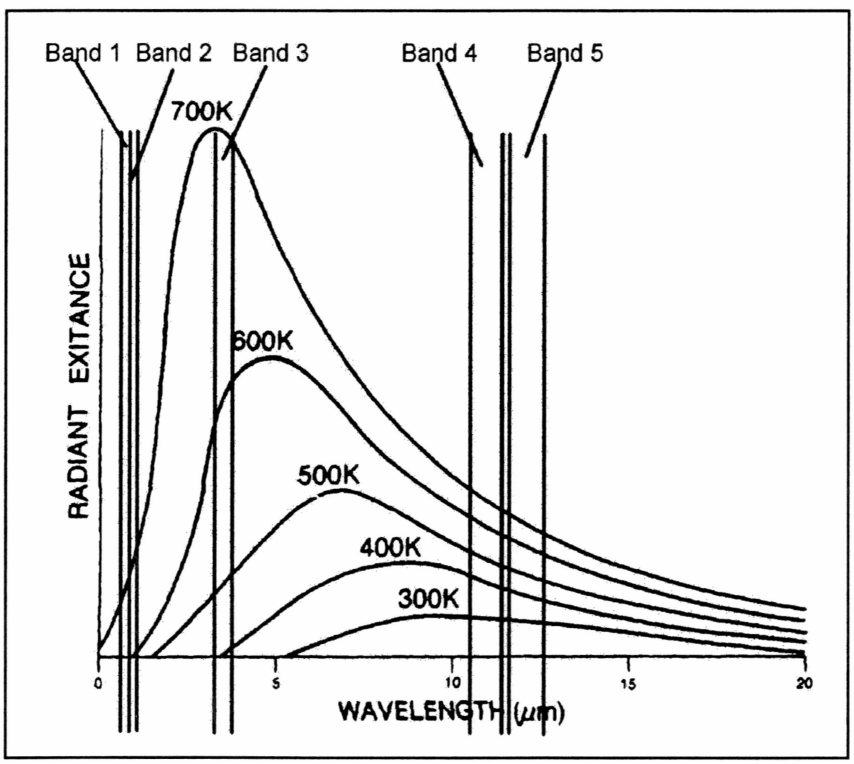

Figure 6. Blackbody radiation curves for specific temperatures and location of AVHRR bands. (Modified from Campbell, 1996).

record data, demonstrating the ability of AVHRR to detect very small volcanic hot targets using this wavelength. The different AVHRR sensors saturate in band 3 at 47-49 °C. Most eruption clouds are also depicted well in band 3. However, because reflected sunlight includes radiation in these wavelengths, analysis of daytime images must be carefully scrutinized. For example, a small meteorological cloud at the summit of a volcano may reflect solar energy in a manner that appears to be elevated surface temperature, because the sunlight reflected by the cloud can give AVHRR measurements similar to those of hot volcanic features. Of course, reflectance is not a problem at night. But at the latitude of Alaskan volcanoes, this is an important phenomenon during the extended daylight hours of long summer days. Another condition that can mimic a volcanic thermal anomaly can occur when a cold meteorological cloud lies just below the summit of the volcano. This condition is common in the fall and early winter, and the relative thermal contrast between the cloud and the summit can make the summit appear much warmer than the surrounding area in the image. Crater lakes, which cool more slowly than the ground around them, will often exhibit significant thermal contrast from the surrounding area, and may give the appearance of a volcanic thermal anomaly.

The band 4 (10.3-11.3-μm) image is examined next. Band 4 measurements are not corrupted by the presence of high temperature pixel components or reflected solar energy, and rarely if ever saturate, giving a true pixel integrated temperature. Only the largest and hottest volcanic features on the ground (lava flows, fountaining, pyroclastic flows) will produce a thermal anomaly that is visually detectable in a band 4 image, and the observation of one in band 4 data is significant. Occasionally eruption clouds are

more easily distinguished in band 4 than band 3; factors which may have a role in this include ash and gas content of the cloud, cloud opacity, and meteorological conditions.

The differences between a band 4 and 5 (11.5-12.5-μm) image are very subtle, and the band 5 image usually does not reveal anything new when viewed beside the band 4 image. However, when combined, they provide one of the key features AVHRR offers to volcano monitoring. Holasek and Rose (1991) showed the utility of subtracting the band 5 value from that of band 4. This is referred to as the split window technique, and takes advantage of the absorption properties of ash clouds at different wavelengths. Ash-rich clouds tend to have a lower signal in band 4 than in band 5, due to absorption of energy at band 4 wavelengths by water and aerosols (Prata, 1989). Thus, negative 4 minus 5 results usually indicate ash-rich volcanic eruption clouds, and positive values are typically associated with ash-free meteorological clouds. Young ash clouds may be transparent at the edge only, and older clouds are often entirely transparent. Using this technique, ash clouds can usually be identified even during overcast conditions.

Band 1 (0.58 - 0.68 μm) and band 2 (0.725 - 1.1 μm) are used primarily to show the location of the coastline and topographical features. Generally band 2 is more useful for this due to better contrast between land and water and slightly increased atmospheric transmission under hazy conditions. The radiation at these wavelengths is almost entirely reflected solar energy. A few instances of vigorous lava fountaining and flow have been detected in band 2 images (Dean et al., 1998). Albedo contrasts between land and water, and between areas of land of different slope directions, are revealed in these images. River drainages, lakes, mountains, ridges, and calderas are often depicted with

remarkable clarity, which is important for interpreting the geographic location of volcanic thermal anomalies when it is not obvious in the other channels. This is a particular problem in band 3 daylight images during overcast or hazy conditions, in which the boundary between land and sea is often obscured by solar reflection. The band 3 and band 1 or 2 image can be "flickered", an image analysis technique in which the same window alternatively displays two or more images. The band 3 thermal anomaly is thus coincident with the volcano visible in the band 1 or 2 image. Band 1 and band 2 images often reveal volcanic water vapor plumes that are not seen in the thermal bands 3, 4, and 5. Because the albedo channels are sensitive almost exclusively to reflected solar radiation, they are of no use in nighttime images.

2.5 The Problem of Variable Satellite Viewing Angle

Mouginis-Mark et al. (1994) addressed the issue of AVHRR viewing geometry when monitoring volcanic thermal anomalies at the Pu'u O'o and Kupaianaha vents at Kilauea Volcano, Hawaii. Of primary interest to their study was the effect of increased pixel size as scan angle increases when observing surface activity on the flanks of basaltic shield volcanoes. In this environment, the only scenario in which topography plays an important role is a lava lake, which could be shielded from the sensor by the crater walls when viewed in a position at some distance from nadir.

However, the tall, steep sided stratovolcanoes common in volcanic arcs present a very different viewing environment. Not only is a summit crater a potential barrier between a thermal anomaly and the sensor, but the volcanic edifice itself can present

awkward viewing geometries not found in the broad, low relief terrain typical of Hawaiian-type shield volcanism.

A component of image processing is resampling, in which the raw data is manipulated to create an image of uniform pixel size and the image data is fitted to a map projection. Nadir pixels are not greatly affected by this, since they are by design already the size sought by the resampling. So a thermal anomaly of one pixel at nadir in a raw image will be approximately the same size in the resampled image. As the pixel size increases with viewing angle and distance from nadir, a raw pixel may be duplicated into two or more resampled pixels. Thus if a thermal anomaly is of sufficient size and temperature to saturate a single off nadir pixel, it may be represented by several saturated pixels in the resampled image. This exaggeration must be taken into consideration when the size of the thermal anomaly is measured.

The effect of resampling on the number of anomalous pixels in AVHRR imagery was studied using data from the Kliuchevskoi eruption, and is illustrated in figures 7, 8, and 9. Figure 7 shows the number of saturated band 3 pixels (where the signal exceeds the upper limit of the detector, about 47 °C) plotted against the satellite scan angle, for the corresponding native (not resampled) and resampled images, from 24 images of the Kliuchevskoi eruption that featured saturated pixels. A scan angle of zero degrees is a nadir view; 50 degrees approaches the maximum off-nadir view.

At low scan angles (zero to 20 degrees) there are generally more saturated pixels in the raw image than in the resampled image. This is an effect of the resampling method, which calculates the value of the resultant pixel from a neighborhood of original

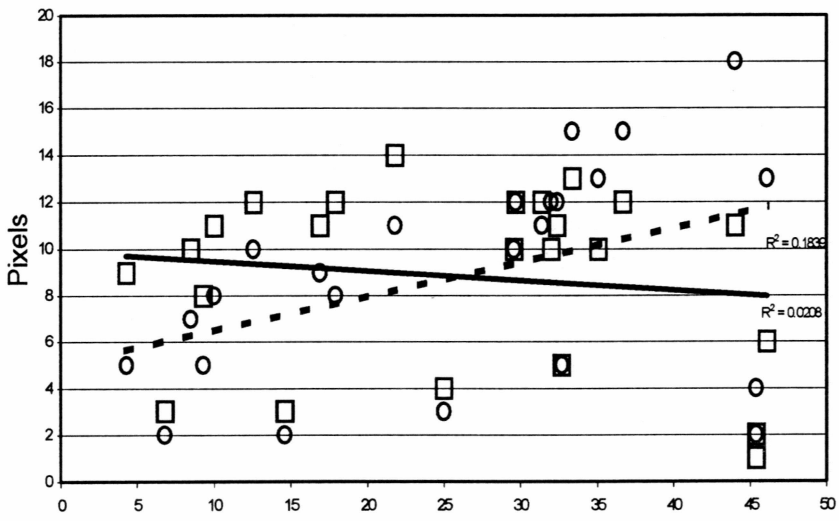

Figure 7. Saturated band 3 pixels vs. scan angle, raw and resampled. Y-axis is number of saturated pixels observed in the raw (not resampled) and resampled versions of the data.

pixels. The resampling dilutes and distributes, or smears, the anomalously high value over several pixels. This assigns lower values to each pixel, and can partially or completely mask the anomaly.

At high scan angles (35 to 50) there are more saturated pixels in the resampled image (figure 7). Though the smearing effect probably occurs here as well, the multiplication of pixels that occurs (creating uniform 1.1-km pixels from the larger ones at the scan edge) offsets and supercedes the smearing effect. This exaggerates the size of the anomaly by creating up to 7 additional pixels with high temperature values not seen in the raw data, artificially doubling the size of the anomaly in some instances. At moderate scan angles, the smearing and multiplication effects are roughly in balance, and the number of saturated pixels is similar in the two versions of the data.

The effect of pixel multiplication is also shown in figure 8, where the number of sensor recovery pixels (defined on page 30 below), is exaggerated in resampled images acquired at high scan angles.

Figure 9 shows a general relationship between the maximum temperature measured with channel 4 in the raw image, and sensor scan angle. At higher scan angles the tendency is for the maximum anomaly temperature to be lower than at low scan angles. This is to be expected, since the raw pixel size varies from 1.21 square km at nadir to more than 11 square km at the maximum viewing angle. At high scan angles the same hot feature will occupy a smaller fraction of the pixel. The high-angle anomaly will thus have smaller influence on the integrated temperature, and the measured temperature

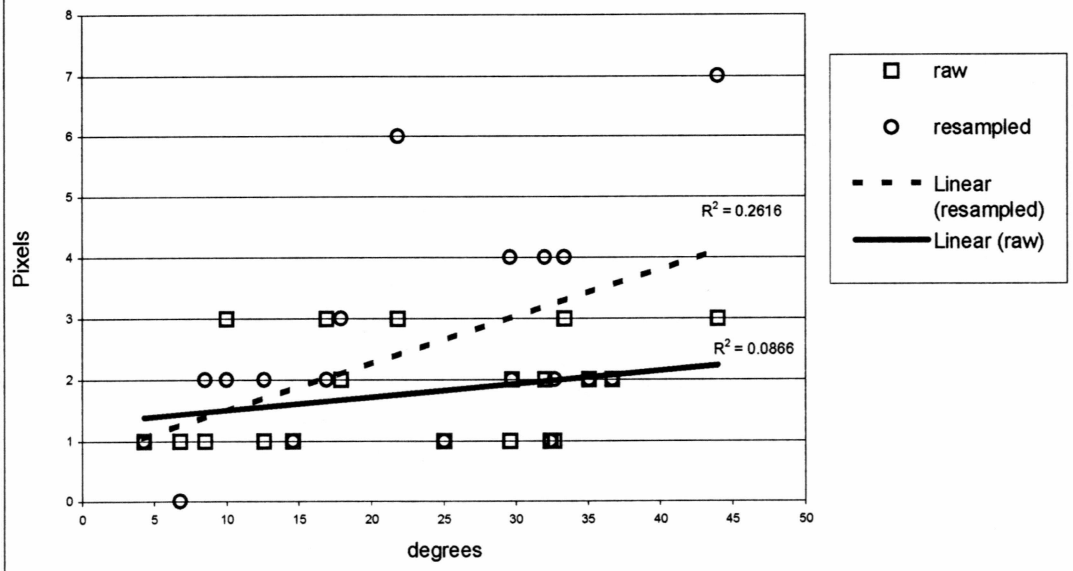

Figure 8. Band 3 sensor recovery pixels (SRPs) vs. scan angle, raw and resampled. Y-axis is the number of SRPs observed in the raw (not resampled) and resampled versions of the data.

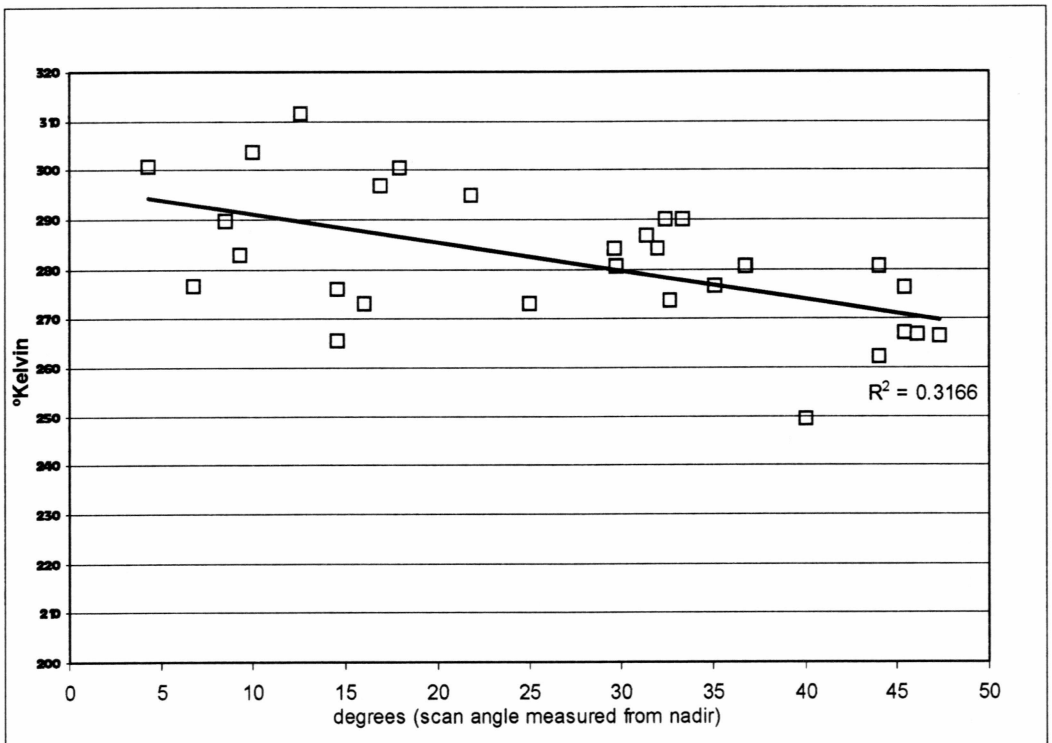

Figure 9. Band 4 maximum temperature vs. scan angle. Lower temperatures at high scan angles are due to increased size of the ground sample area decreasing the relative radiance contribution of the hot feature.

will be lower. This effect should be considered when using maximum temperature values as measures of fluctuating activity.

The problem in image interpretation and analysis caused by resampling is further exacerbated in areas of high relief. The resampling algorithm assumes that the earth is a smooth sphere or geoid. If the thermal anomaly is on the steep flanks of a volcano facing the sensor, the area it occupies is not as large as the flat area beyond the volcano that the resampling process assumes it is viewing. This phenomenon was observed during monitoring of the 1996 eruption of Pavlof Volcano on the Alaska Peninsula. A channeled spatter-fed agglutinate flow extended from the summit several km down the west flank of the volcano. Images in which the volcano was near nadir depicted the flow to be approximately this length. When nadir was west of the volcano, and the sensor was looking east and along the flow axis, however, the aspect ratio of the feature increased during resampling, and the flow appeared in the resampled image to be up to 15 km in length. In images viewed by the sensor from the east (west of nadir), the direction of elongation of the anomaly was observed to change by 90°, from northwest-southeast to northeast-southwest. The reason for this variation is not understood, though smaller vents on the north and east edges of the summit may have contributed to the size of the anomaly when viewed from the east. This was rather confounding during initial stages of the eruption when there was no ground truth to accompany the remotely sensed information.

While fitting the image data to a map projection is essential for creating a visual effect, the uncertainty and data homogenization introduced by the resampling method

must be considered when the data are used in quantitative analysis. Since volcanic thermal anomalies in this study were in all likelihood much smaller than the pixels in the image, any artificial exaggeration of the anomaly will be significant. This is not problematic when observing large homogeneous targets such as the ocean surface or sea ice, where the individual pixels are not scrutinized. Therefore, to avoid the potential misrepresentation of the conditions on the ground where the volcanic thermal anomalies are observed, raw HRPT AVHRR data were used for quantitative analysis in this study.

2.6 Sources of Error

Several factors make quantitative analysis of volcanic thermal anomalies more challenging by masking measurable temporal change in the eruption. The most critical factor is the variable angle at which the volcano is viewed by the satellite. Not only can this increase the sample size by more than a factor of 10, but the atmospheric path between the source of the radiation and the sensor grows with scan angle as well. This leads to differential scattering and absorption of the emitted radiation before it can be measured. Variable atmospheric composition, especially water vapor, has the same effect. Many volcanoes in Alaska and Kamchatka are composite cones, and the orientation of their steep sides with respect to the sensor also affects the ground sample size. Steep crater walls can act as a barrier between the heat source and the sensor at some viewing geometries.

The temperature values derived from AVHRR data include an assumption that the surface of the earth is a homogeneous blackbody radiator. Though volcanic rocks are

efficient radiators (emissivity >85%), some error is introduced by this assumption. Also, in daytime measurements, solar reflection at the same wavelengths as those in the AVHRR thermal channels will contribute to the radiance collected by the sensor, and influence derived temperature values.

Chapter 3: Attributes For Analysis In This Study

3.1 Introduction

This section defines the attributes which were extracted from each AVHRR image and used in quantitative analysis and/or temporal profiling. These features are indicative of the intensity of unrest at the volcano as expressed in thermal characteristics, and provide different methods of quantifying the level of volcanic activity using AVHRR imagery.

3.2 Maximum Temperature

The maximum temperature measured by bands 3 and 4 can be monitored from image to image and used to assess the general state of unrest at a volcano as expressed in the thermal data.

3.3 Threshold Pixels

A threshold of 35 °C (308 °K) is used to discriminate anomalously hot pixels from the background data in AVHRR band 3 images. This value was chosen somewhat arbitrarily, and lies between ambient terrestrial temperatures and the saturation level of the sensor (see below).

3.4 Saturated Pixels

Band 3 is extremely sensitive to emitters at pyroclastic temperatures (figure 6). In most of the data sets in this study one or more pixels are saturated, having reached the maximum temperature that the sensor can register. The saturation temperature, or

maximum reported value, varies around 48 °C (321 °K) between the AVHRR sensors carried on different NOAA satellites, and is defined here as any measurement greater than 47 °C (321 °K).

3.5 Sensor Recovery Pixels

Harris et al. (1995b) described a phenomenon observed in AVHRR band 3 data from Etna and Stromboli volcanoes called "sensor recovery pixels". Attributed to a faulty sensor response, these are defined as areas of anomalously low temperature values which often occur immediately down-scan from a high temperature thermal anomaly that saturates or nearly saturates one or more pixels (figure 10). Two factors were suggested as controls on the occurrence of sensor recovery pixels (SRPs): distance from nadir of the thermal anomaly, and aerial extent of the thermal anomaly. SRPs were observed during this study at several locations in the Aleutians and Kamchatka as well.

As the distance from nadir increases, the size of the individual pixels increases. So not only does a thermal anomaly viewed near the edge of the swath occupy fewer pixels (Harris et al., 1995b), but anomalies that are of subpixel size occupy a smaller area relative to the pixel size. Thus the radiance of a subpixel heat source in a pixel at the scan edge is diluted by the additional area of ambient temperature within the pixel. The same thermal anomaly, viewed at nadir, has greater influence on the nature of the radiance contributing to the pixel. Thus the presence and number of SRPs is also affected by these parameters.

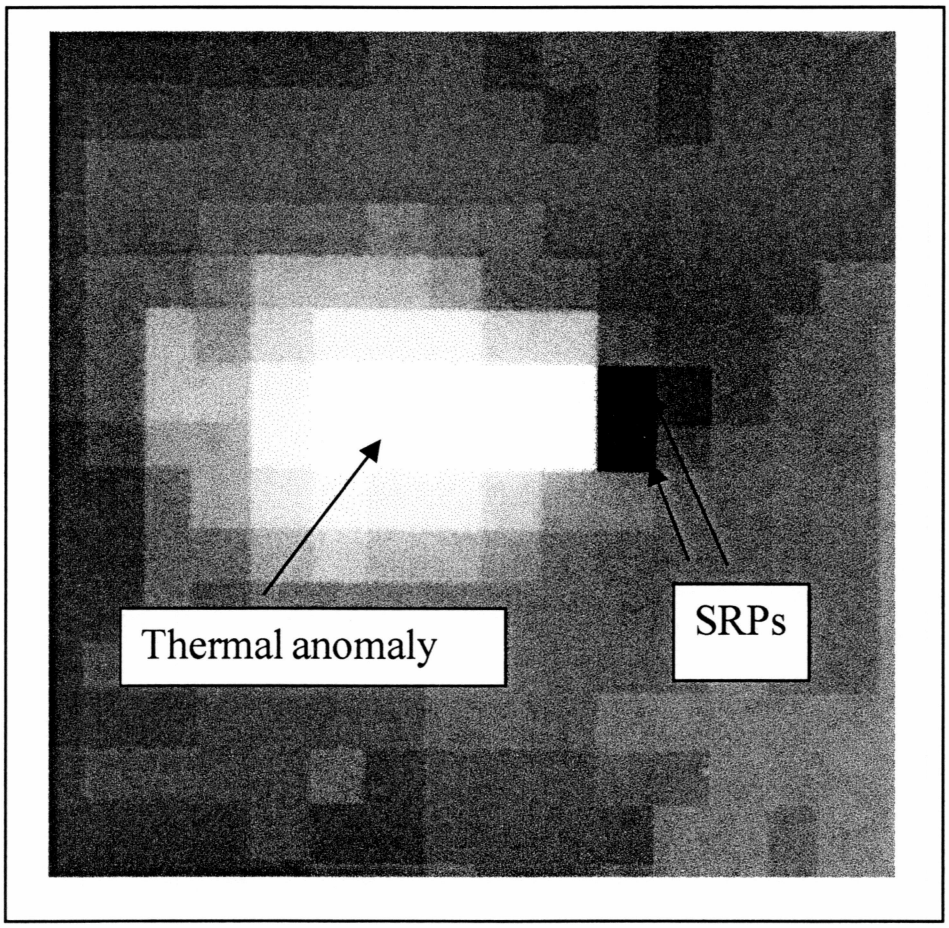

Figure 10. Sensor recovery pixels (SRPs) at Kliuchevskoi on September 10, 1994.

Not all volcanic thermal anomalies are accompanied by SRPs. This is due to the above discussed factors: size of the heat source, temperature of the heat source, and position within the satellite swath. Because of the latter item, the absence of SRPs does not necessarily preclude an anomaly from representing a large and hot feature, such as a lava flow. In at least three instances, the presence of SRPs in an AVHRR image has coincided with on site visual observations of copious amounts of surface lava (Kliuchevskoi and Pavlof in this study, and Etna in Harris et al., 1995b). This suggests that an image of a volcanic thermal anomaly which does have SRPs is very likely to represent a very high temperature feature, such as a surface breakout of lava, a lava flow, lava fountaining, or very hot pyroclastic flow, and not fumarolic activity, cooling inactive lava, thermal heating of inactive lava, or reflected solar illumination during daylight hours. With this in mind, when SRPs are observed in an AVHRR image of a volcano during routine monitoring, it is interpreted to indicate effusion of lava or pyroclastic material.

3.6 Total Volcanic Signal

The "total volcanic signal" (TVS) technique for quantifying variations in eruption intensity is described by Wooster and Rothery (1997), wherein the radiance of all pixels more than 2 σ above the background temperature in the area of the volcano is summed. This approach incorporates the area of the anomaly as well as the intensity of the radiance of each anomalous value. However, in the raw data, this involves summing the temperature of pixels of different sizes. This method was applied to the Kliuchevskoi eruption dataset with a modification, which is described below.

The AVHRR data acquired over a volcanic thermal anomaly often falls into two nearly distinct populations with few intermediate values: uniform background, and uniform anomaly. The anomaly temperature thus defines the standard deviation, and often no value approaches 2 σ greater than the mean background temperature, though the anomaly is obvious. This is particularly true of band 3 data, where the anomalous values cluster at or near saturation temperature against a relatively uniform background of subfreezing temperatures. To include as much of the anomaly in quantitative analysis as possible, 1.5 σ is used to define the anomaly in band 4, and a threshold value of 35 °C (308 °K) defines anomalies in band 3.

In several instances zero volcanic signal was calculated for observations in either band 3 or band 4, but not both. A third quantity, "TVS7", is defined here as the sum of the TVS in band 3 and 4, and serves to smooth the effect of a zero TVS measured in one of the thermal band when the eruption was ongoing. This incorporates the sensitivity of band 3 to small hot features, and the reliability of band 4 to give true pixel integrated temperatures over larger areas.

3.7 Total Volcanic Wattage

The temperature values used in describing AVHRR data are derived from the radiance of the measured surface that reaches the sensor. In the study of volcanic thermal anomalies, where the heat source is usually much smaller than the pixel, it may be more appropriate to use those radiance values to calculate a basic physical quantity to use in quantitative analysis of temporal change, rather than reporting measurements in

unreasonably large temperature values as is done in TVS. From the temperature values given by the AVHRR data, the total emitted radiation W in watts per square meter can be calculated using the Stefan-Boltzman law:

$$W = \sigma * T^4,$$

where σ is the Stefan-Boltzman constant [$(5.6697 \pm 0.0029) * 10^{-8}$ W m^{-2} K^{-4}] and T is the temperature in degrees K (Lillesand and Kiefer, 1994). In addition, the area of the raw data anomaly in square meters can be calculated using the number of anomalous pixels and the pixel size at that scan angle. By combining the area of the anomaly with the radiance, the relative magnitude of the thermal anomaly at the time of the observation can be estimated in watts.

Chapter 4: The 1994 Kliuchevskoi Eruption

4.1 Introduction

Kliuchevskoi Volcano is located at 56° 03' N 160° 39' E on the Kamchatka Peninsula in eastern Russia (figure 1). It is the tallest active volcano in Eurasia, reaching an altitude of 4835 m (figure 11). Kliuchevskoi is the most active volcano in Kamchatka, having erupted 89 times between 1697 and 1998 (Simkin and Siebert 1994).

The 1994 eruption began on September 8 at 0400 UT according to KVERT seismic records and reached a paroxysmal phase on October 1 (GVN Bulletin, v.19, number 8, August 1994). AVO began using AVHRR to monitor Kliuchevskoi on September 11 in response to reports of the eruption; analysis of earlier images was carried out retrospectively using HRPT data from the UAFGI ADVAL data archive.

4.2 Pre-eruption Chronology

More than 150 satellite passes potentially covering the Kliuchevskoi area between August 14 and October 15 1994 were analyzed (table 1). Many of these failed to depict the volcano due to meteorological clouds obscuring the volcano, missing scan lines or noise errors in the satellite data, or the coverage being truncated due to satellite tracking errors since the area is near the edge of the UAFGI receiving station mask.

A cloud-free image from August 15 at 1836 UT clearly depicted the area of Kliuchevskoi Volcano, and no thermal anomaly or eruption cloud is present (figure 12). This is the latest cloud-free image acquired prior to observation of eruptive activity. British climbers who reached the summit in early August observed no unusual activity

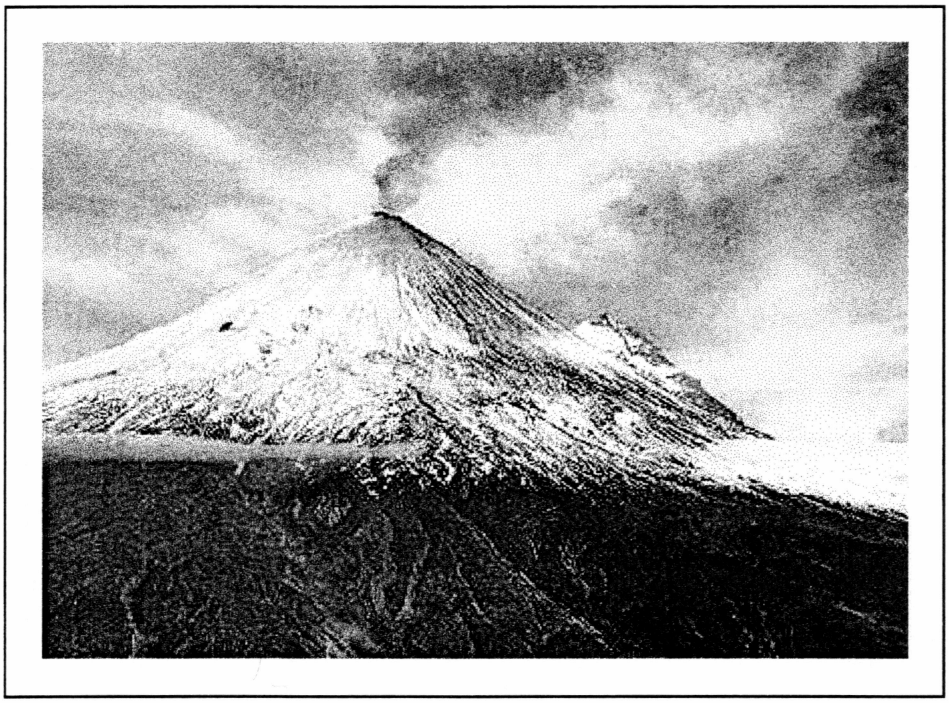

Figure 11. Photograph of Kliuchevksoi Volcano (VolcanoWorld 2000).

date	image		date	Image		date	image	
14-Aug	N12.94226.2111		5-Sep	n12.94248.2135		29-Sep	n12.94272.0727	*
15-Aug	N11.94227.0459		6-Sep	n12.94249.0724		29-Sep	n12.94272.2115	*
15-Aug	n12.94227.0700		6-Sep	n12.94249.2113		30-Sep	n12.94273.0705	*
15-Aug	n11.94227.1854		7-Sep	n12.94250.0703		30-Sep	n12.94273.2054	*
17-Aug	n12.94229.2146		7-Sep	n12.94250.2051		1-Oct	n12.94274.0653	*
19-Aug	n11.94231.0410		8-Sep	n11.94251.0506	*	1-Oct	n10.94274.2017	
20-Aug	n12.94232.0652		8-Sep	n12.94251.0641	*	1-Oct	n12.94274.2032	*
20-Aug	n12.94232.1933		8-Sep	n12.94251.2030	*	1-Oct	n12.94272.2212	
20-Aug	n11.94232.2041		8-Sep	n11.94251.2210		2-Oct	n10.94275.1953	*
21-Aug	n12.94233.2019		9-Sep	n11.94252.0454	*	2-Oct	n12.94275.2151	
21-Aug	n12.94233.2159		9-Sep	n11.94252.2028		2-Oct	n10.94276.0541	
22-Aug	n11.94234.1908		9-Sep	n12.94252.2148		3-Oct	n10.94276.1929	
22-Aug	n11.94234.1908		10-Sep	n11.94253.0441		3-Oct	n12.94276.2129	
22-Aug	n12.94234.2138		10-Sep	n12.94253.0738	*	4-Oct	n10.94277.0517	
23-Aug	n11.94235.0502		10-Sep	n11.94253.1836	*	4-Oct	n12.94277.2107	
23-Aug	n11.942351856		10-Sep	n11.94253.2016		5-Oct	n12.94278.2045	
23-Aug	n12.94235.2116		10-Sep	n12.94253.2127		6-Oct	n12.94279.0609	
24-Aug	n11.94236.0449		11-Sep	n11.94254.0429	*	6-Oct	n10.94279.1956	
24-Aug	n12.94236.0706		11-Sep	n11.94254.1823		6-Oct	n12.94279.2204	
24-Aug	n12.94236.2054		11-Sep	n11.94254.2004		7-Oct	n10.94280.0545	
25-Aug	n11.94237.0437		11-Sep	n12.94254.2105		7-Oct	n12.94280.0614	
25-Aug	n11.94237.1831		12-Sep	n11.94255.1952		7-Oct	n10.94280.1932	
26-Aug	n11.94238.0425		12-Sep	n12.94255.2043		8-Oct	n10.94281.0521	
26-Aug	n12.94238.2151		13-Sep	n11.94256.1939		8-Oct	n12.94281.0732	
27-Aug	n12.94239.2130		13-Sep	n12.94256.1939		8-Oct	n10.94281.1908	
28-Aug	n12.94240.0719		14-Sep	n12.94257.2140		8-Oct	n12.94281.2121	
28-Aug	n12.94240.2108		15-Sep	n10.94258.0615		9-Oct	n10.94282.2024	
29-Aug	n12.94241.0658		15-Sep	n12.94258.0730		9-Oct	n12.94282.2059	
29-Aug	n12.94241.2046		15-Sep	n10.94258.2003		10-Oct	n10.94283.0613	
30-Aug	n11.94242.0516		15-Sep	n12.94258.2118	*	10-Oct	n12.94283.0649	
30-Aug	n12.94242.0636		16-Sep	n10.94259.0551	*	10-Oct	n12.94283.2037	
30-Aug	n11.94242.1911		16-Sep	n12.94259.0708	*	11-Oct	n10.94284.0548	
30-Aug	n12.94242.2024		16-Sep	n12.94259.2057	*	11-Oct	n12.94284.0627	
30-Aug	n12.94242.2205		19-Sep	n10.94262.0619	*	11-Oct	n10.94294.1936	
31-Aug	n11.94243.0504		19-Sep	n12.94262.0744		11-Oct	n12.94284.2156	
31-Aug	n11.94243.1858		20-Sep	n10.94263.0554	*	12-Oct	n10.94285.0524	
31-Aug	n12.94243.2143		20-Sep	n12.94263.0721	*	12-Oct	n10.94285.1912	
1-Sep	n12.94244.0733		20-Sep	n12.94263.2110	*	12-Oct	n12.94285.2134	
1-Sep	n11.94244.1846		21-Sep	n12.94264.0700	*	13-Oct	n12.94286.0724	
1-Sep	n11.94244.2026		21-Sep	n12.94264.2049	*	13-Oct	n10.94286.1847	
1-Sep	n12.94244.2121		22-Sep	n12.94265.2207		13-Oct	n10.94286.2028	
2-Sep	n11.94245.0439		22-Sep	n12.94265.0638	*	13-Oct	n12.94286.2112	
2-Sep	n12.94245.0711		22-Sep	n12.94265.2027		14-Oct	n12.94287.0524	
2-Sep	n11.94245.1833		23-Sep	n12.94266.2145		14-Oct	n10.94287.1823	
2-Sep	n12.94245.2100		24-Sep	n12.94267.0735	*	14-Oct	n10.94287.2004	
3-Sep	n11.94246.0427		24-Sep	n12.94267.2124	*	17-Oct	n12.94290.0737	
3-Sep	n11.94246.0649		25-Sep	n12.94268.0713	*	18-Oct	n12.94291.0715	
3-Sep	n12.94246.2038		26-Sep	n12.94269.0652		19-Oct	n12.94292.0654	
4-Sep	n11.94247.0415		26-Sep	n12.94269.2040	*	20-Oct	n10.94293.0532	
4-Sep	n11.94247.1809		27-Sep	n12.94270.2159		22-Oct	n12.94295.0729	
4-Sep	n11.94247.1949		28-Sep	n12.94271.2137		24-Oct	n10.94297.0535	
						24-Oct	n12.94297.0645	

Table 1. AVHRR images used in this study. Highlighted images were used in thermal anomaly analysis, and chosen for limited cloud cover.

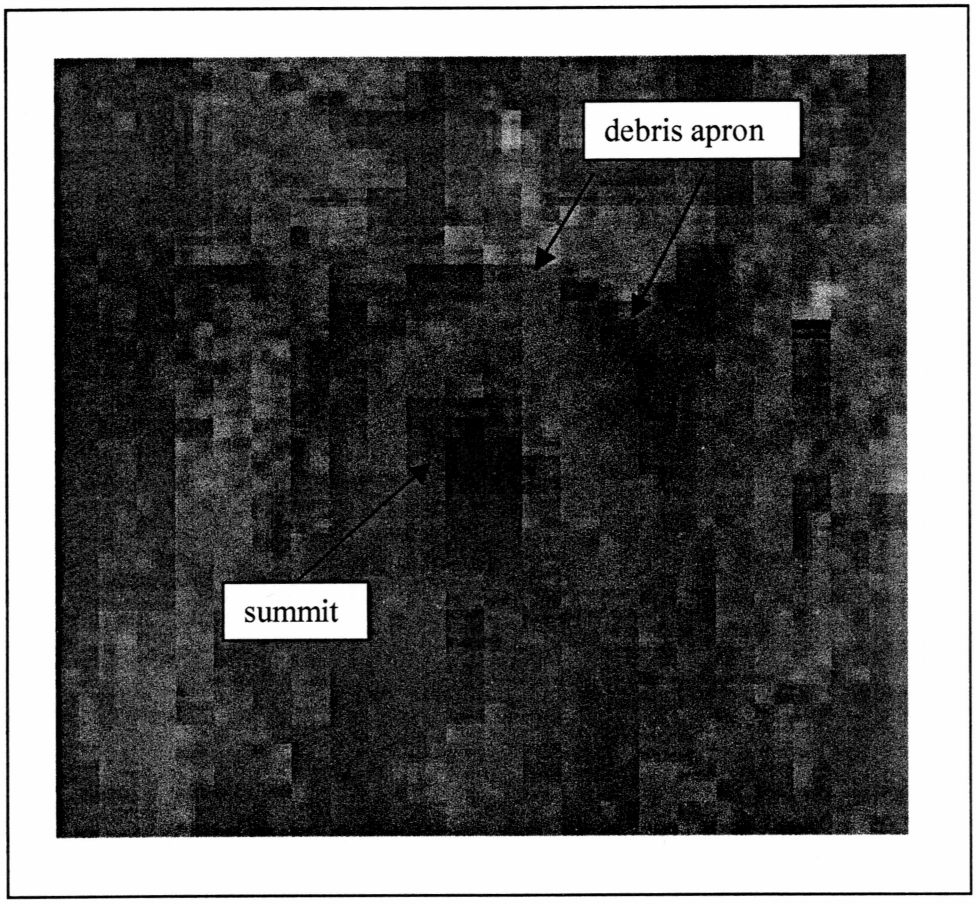

Figure 12. AVHRR band 3 image from August 15, 1994. No thermal anomaly is observed at the summit of Kliuchevskoi. Image is GAC data (4.4 km pixels) from the NOAA Satellite Active Archive.

(BGVN 1994). This indicates that surface expression of the impending eruption was evident no sooner than August 16.

Between August 15 and September 8 the summit of Kliuchevskoi was obscured by clouds in most of the images acquired. On August 31 and September 1 the peak was visible above the cloud tops, and no thermal anomaly was observed. Possible subtle anomalies appeared in images from September 4 and 6, though the maximum temperature of these was well below saturation levels of the band 3 sensor.

On September 8 a distinct change in the thermal conditions at the summit was observed. An image received at 0506 UT showed the summit of Kliuchevskoi above the cloud cover, with maximum band 3 temperatures near saturation in the upper 40s °C (figure 13). This AVHRR measurement was made approximately one hour after the eruption began according to seismic records. Lava fountaining and outbursts of gas and ash were reported by ground observers on September 8 as well. The report of incandescent material at the surface coincides with the strong thermal anomaly observed in satellite images. This image was the earliest to be included in the quantitative analysis that follows.

4.3 Additional Observations of the Eruption

The eruption was characterized by frequent gas and ash outbursts, lava fountaining and multiple lava flows, continuous volcanic tremor, and phreatic explosions (BGVN 1994). Tremor amplitude increased during the course of the eruption, from 6.3

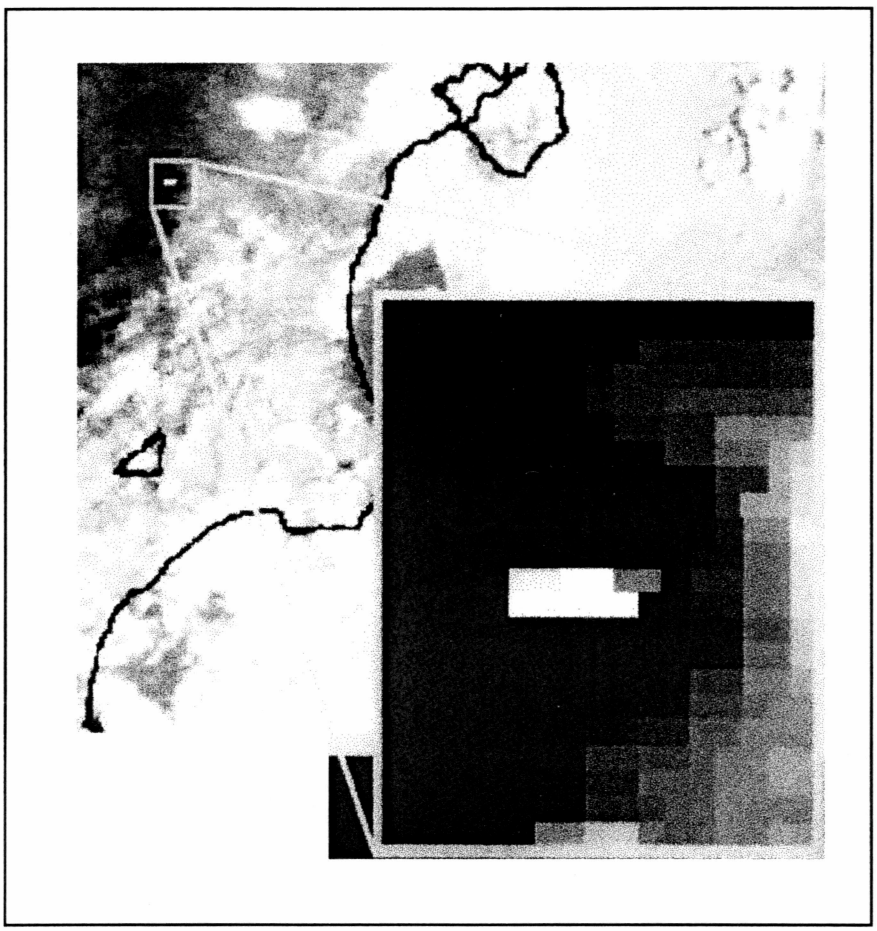

Figure 13. Thermal anomaly observed at Kliuchevskoi on September 8, 1994.

μm on September 14 to 8.4 μm on October 1. Reports of lava fountaining show that fountain heights increased throughout the eruption, at 200-300 meters on September 8, 300-500 meters above the crater during September 15-19, 500-700 meters between September 20-23, and 900 meters on October 1, with bursts to 4500 m above the crater (BGVN 1994). The height of the eruption column remained around 2-3 km above the crater during much of the eruption, until the paroxysmal phase began on September 30. Column height increased from 10 km on September 30 to 15-20 km on October 1 (BVGN 1994).

4.4 Temporal Analysis of the Volcanic Thermal Anomaly

Twenty-nine cloud-free images from September 8 to October 3 were chosen for analysis (table 1). A seven by seven pixel grid centered at the volcano summit was extracted from the AVHRR scene for quantitative analysis. The sensor data was automatically calibrated to temperature, but not fitted to a map projection or resampled. Six attributes were measured and the temporal variation in these attributes is shown in figures 14 -16.

4.4.1 Maximum Temperature

Figure 14 shows the temporal variation in maximum temperature measured in channels 3 and 4 for each of the 29 images. This highlights the general state of unrest at the volcano, but does not consider the areal extent of the activity. The band 3 measurements show that at least one pixel was saturated at around 320 °K for much of the

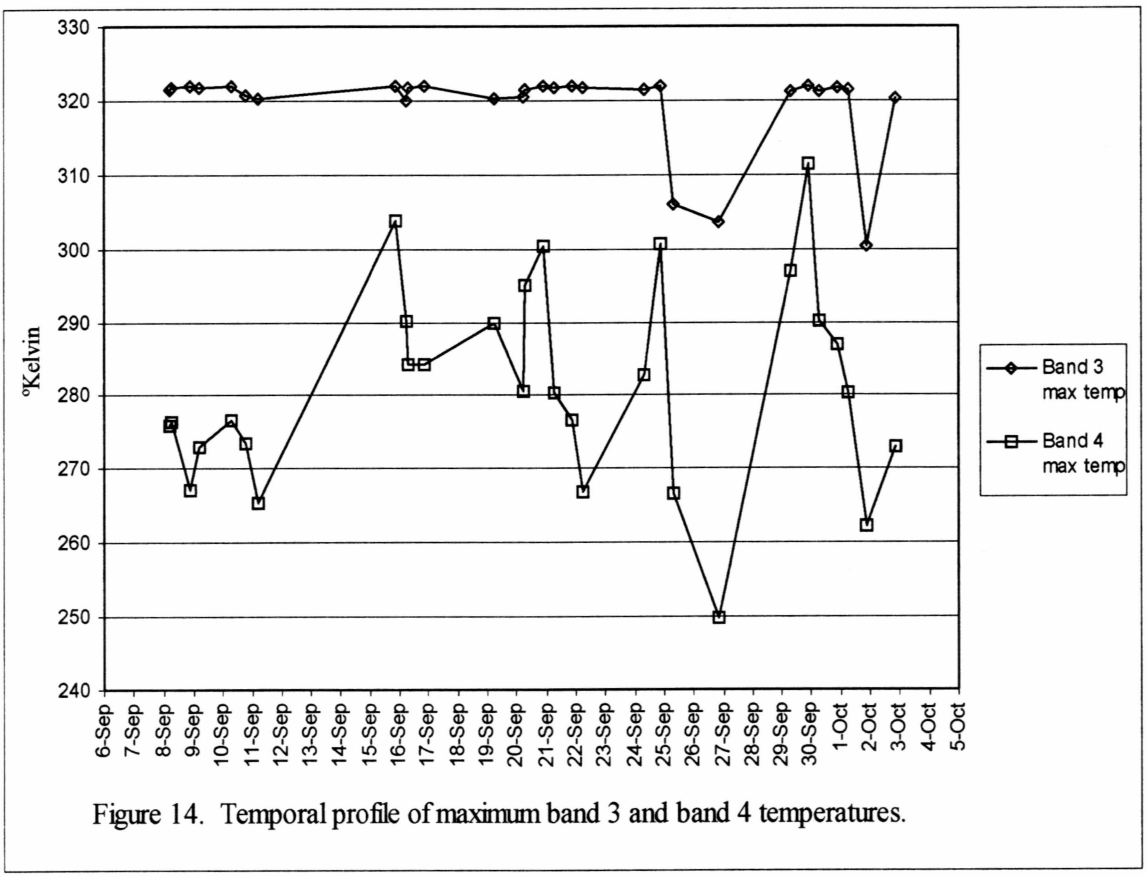

Figure 14. Temporal profile of maximum band 3 and band 4 temperatures.

eruption period between September 8 and October 2, indicating a sustained high level of activity. A distinct decrease in the band 3 maximum temperature occurred around September 25. This was sustained in two observations made between September 25 and 27, followed by a return to saturation temperatures on September 29. Saturation conditions remained through the paroxysmal phase ending October 2 (figure 15).

The channel 4 measurement series in figure 14 shows greater variation in maximum temperature measured at Kliuchevskoi during the eruption. This may indicate changes in the level of activity that were not detected by channel 3 due to its saturation near 320 °K. The minimum that appeared on September 25 is visible in the channel 4 image as well. The maxima in the band 4 measurements occur at a wide range of scan angles. Some coincide with near-nadir views of the volcano, in which the ground sampled by each pixel is smaller, such that the heat source will have greater influence and raise the temperature value as discussed previously.

4.4.2 Saturated Pixels, Threshold Pixels, Sensor Recovery Pixels

In figure 16 the temporal variation of three attributes of the channel 3 data (not resampled) is shown: number of saturated pixels (T3 > 47 °C), pixels exceeding the 35 °C threshold, and sensor recovery pixels (SRPs). This method of pixel counting incorporates the areal extent of the anomaly, and shows considerably more variation in the nature of the volcanic activity during the eruption than is shown in the channel 3 temperature series in figure 14. In figure 16 several episodes during the eruption are recognizable in both the saturated and threshold series. Maxima are observed on

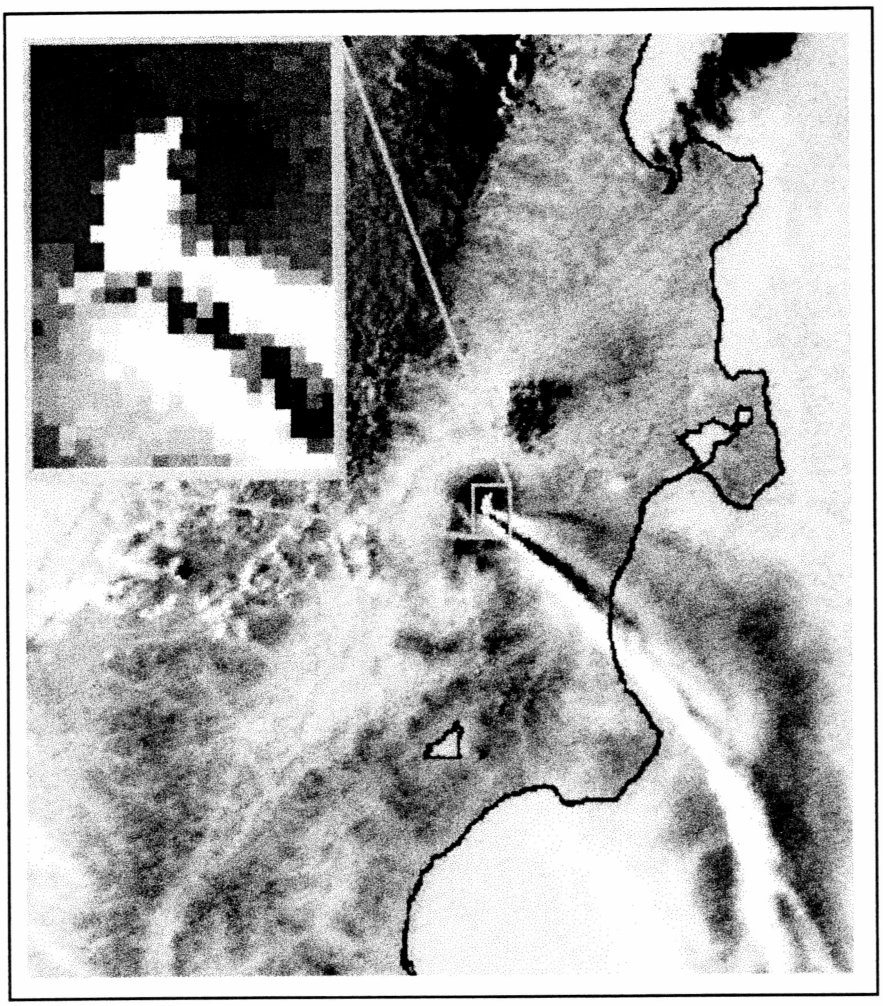

Figure 15. AVHRR band 3 image from October 1, 1994. Thermal anomaly and eruption cloud are visible.

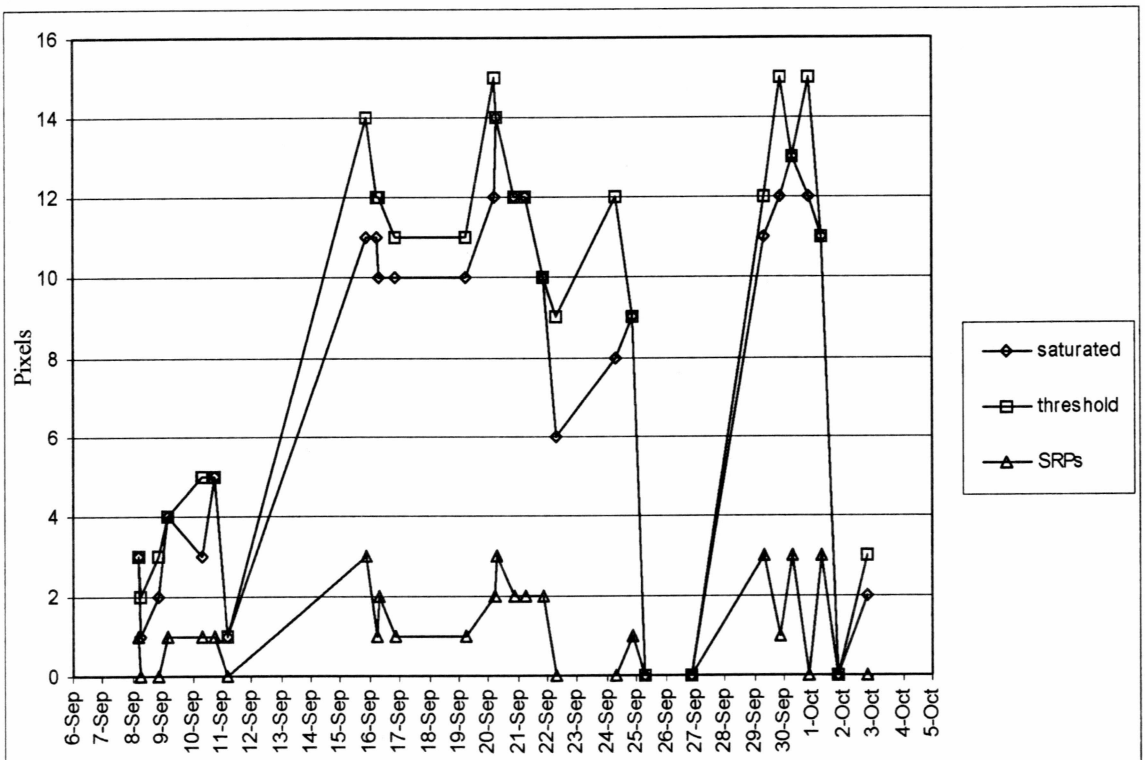

Figure 16. Temporal variation in band 3 attributes. Y-axis is the number of pixels meeting the attribute criteria.

September 10, 15, 20, 24, and 29, separated by measurements of lower magnitude. The SRP series is approximately parallel to the other two, with lower amplitude. These three attributes are most useful for qualitative monitoring of the intensity of the eruption from day to day, and for identifying brief periods of quiescence that may precede more vigorous phases.

4.4.3 Total Volcanic Signal

The temporal variation of TVS3, TVS4, and TVS7 during the eruption, calculated using the method adapted from Wooster and Rothery (1997), is shown in figure 17. Here the episodes of greater activity are recognized as maxima in the series, separated by lower intensity periods at the minima. The highest intensity periods on September 20 and September 30 coincide with observations of continuous volcanic tremor of 8.2 and 8.4 μm, respectively, the maximum tremor values reported during the eruption (GVN 1994).

4.4.4 Total Volcanic Wattage

Figure 18 shows the total anomaly wattage calculated from TVS3, TVS4, and TVS7. Ten maxima are apparent throughout the eruption. One feature is that the two highest intensity maxima appear on September 22 and October 1, slightly offset from those seen in figure 17. The October 1 maxima in figure 18 represents data acquired at 0653 UT; this corresponds well with the GVN report of the initiation of the paroxysmal stage at 0600. The maxima in this series may be exaggerated by scan angle periodicity

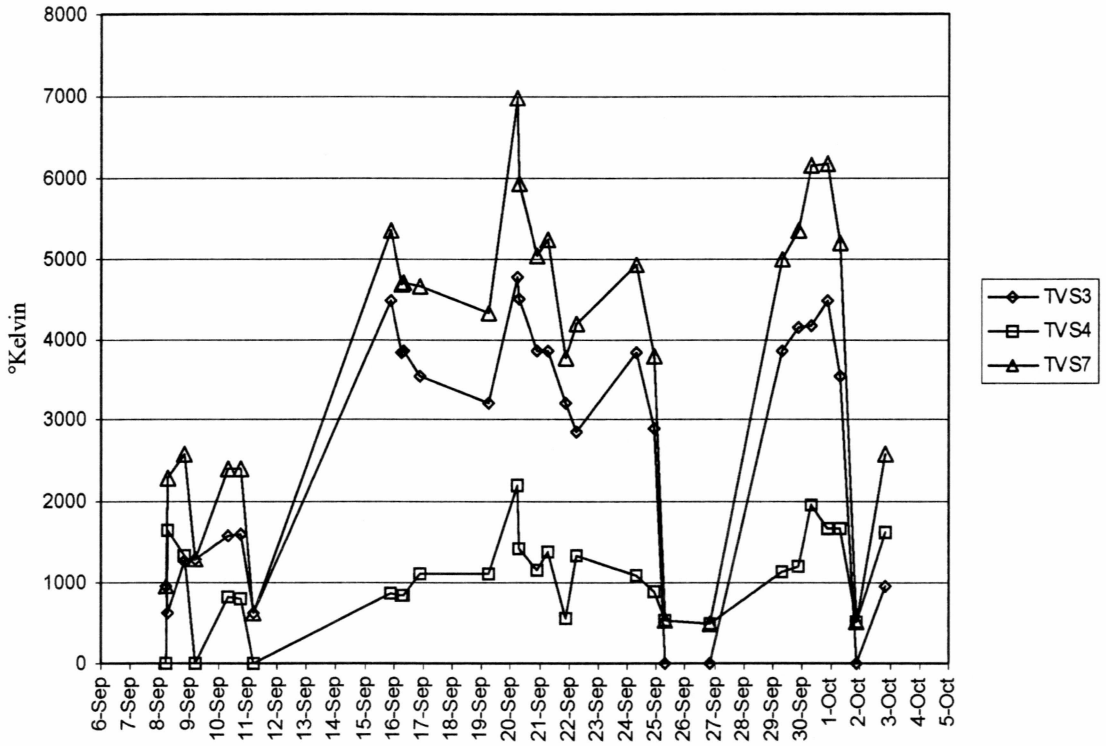

Figure 17. Temporal profile of total volcanic signal in bands 3, 4, and 3+4. Y-axis is the sum of the temperatures of the anomalous pixels.

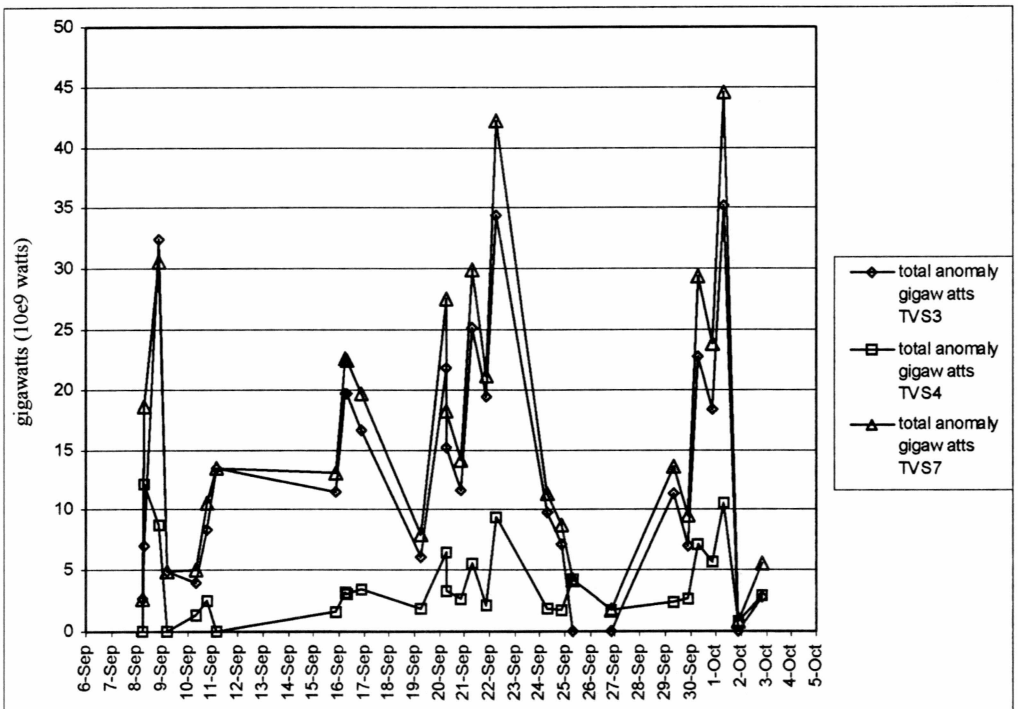

Figure 18. Total volcanic anomaly wattage in bands 3, 4, and 3+4. Y-axis is the sum of the wattage of the anomalous pixels.

effects, as several of them are closely followed by sharp declines in wattage, often separated from the adjacent maxima by only one or two observations.

Chapter 5: Discussion

The effect of resampling image data in which the feature of interest is often smaller than the picture elements is apparent in figures 7, 8, and 9. The dilution of the signal at low scan angles and the exaggeration of the signal at large scan angles make suspect the quantitative analysis of volcanic thermal anomalies using resampled data. Other resampling methods (nearest neighbor or bilinear) may be kinder to radiometric fidelity of the data than the cubic convolution method used here. Further study is required to evaluate these.

Temporal analysis of the maximum band 3 temperature shows sustained levels of saturation or near saturation temperatures from September 8-25. A distinct decrease occurred on September 25, and lower temperatures persisted until September 29, when saturation conditions resumed during the paroxysmal phase that ended the eruption. This recognizable period of quiescence prior to the most violent phase of the eruption may indicate the utility of AVHRR for identifying thermal indicators of a pending plinian phase, even after weeks of sustained intermediate levels of unrest.

Using the maximum temperature in AVHRR channel 3 data to assess the nature of a volcanic thermal anomaly is qualitative at best. The data tends to be saturated by even the smallest area of hot pyroclastic material or lava, and little information can be gained beyond erupting vs. not erupting. But the same sensitivity that makes it less useful for quantitative analysis makes it an excellent indicator of quiescence vs. unrest.

Temporal analysis of the maximum band 4 temperature shows greater variation in summit temperatures than is seen in the band 3 temperature profile. The band 4 series in

figure 14 shows maxima on September 15, 20, 24, and 29. These likely represent episodes of greater intensity during the overall eruptive period. The decrease in band 4 temperature on September 25 coincides with that seen in band 3, and further indicates that there was a lull in activity prior to the ash-producing phase that began on September 29.

By counting the pixels that meet certain criteria associated with unrest, an idea of the areal extent of the thermal anomaly can be developed and used to help assess the magnitude of the activity. Total numbers of saturated and threshold-exceeding pixels in a channel 3 measurement generally indicate the same status of the anomaly (figure 16). The threshold model captures more area in most cases, since it will include anomalous pixels that did not saturate but still reflect the elevated temperature caused by the activity. The presence of sensor recovery pixels is always an indicator of very high temperature targets on the ground, and this feature is best suited for qualitatively assessing the general state of the unrest. For example, given two hypothetical thermal anomalies that are similar in all parameters (viewing angle, maximum temperature, etc.) except the presence of SRPs (one with and one without SRPs), the one that features SRPs is interpreted to indicate with greater certainty that incandescent material is at the surface.

The total volcanic signal profile (figure 17), particularly the TVS7 series, reveals the maxima in intensity at September 15, 20, 24, and 29 also seen in figures 14 and 16. Episodes of relatively higher amplitude are seen in the earliest days of the eruption in this series, though the minima are defined by only one measurement. The highest TVS7

value is observed on September 20, in contrast to the other figures indicating maximum intensity beginning September 29.

The pronounced trough in maximum band 3 and band 4 temperatures shown in figure 14 on September 25 is also observed in the total volcanic signal analysis in figure 17. This may represent a period of relative quiescence at the surface due to a constriction of the volcanic conduit. This constriction may have caused a buildup of energy that was later released in the most violent phase of the eruption, beginning September 29. Alternatively, the decrease in temperature measured during this phase may be due to atmospheric conditions or sensor constraints.

The total volcanic wattage analysis is an attempt to quantify the eruption in terms of a physical property, describing the variable flow of energy during the eruption (figure 18). The difference in shape between the data series shown in figures 17 and 18 is the result of incorporating the area of the pixels into the calculation. Although the wattage value is likely influenced by the viewing geometry even in the raw (not resampled) data, it does indicate an episodic pattern within the larger eruption period, as seen in the other analyses. However, the maxima appear to be offset slightly in the wattage analysis compared to the TVS or other data series. This is believed to be a product of the viewing geometry variation, though further study is needed to better explain this observation.

Because band 4 most accurately measures the pixel-integrated radiance, the wattage values calculated from band 4 data will more realistically describe conditions on the ground. The wattage model produced a maximum on October 1 that best coincided with GVN reports of the paroxysmal phase initiation, as indicated by the highest level of

volcanic tremor during the eruption and the largest ash plume. Although the maxima do not share high scan angle values, the periodicity of this data series may be influenced by the repeating cycle of viewing angle, and this must be considered when analyzing the subtle highs and lows shown in the curve.

Refinement of the TVS and wattage analysis methods could lead to an eruption intensity scale based on AVHRR radiance measurements. Such a scale will provide a standard for comparison of thermal anomalies during the same eruption, as well as comparing anomalies at different volcanoes. By standardizing the quantification of volcanic thermal anomalies, these features can be included with seismic data and other observations in volcanic unrest assessments.

The most significant application of these observations is the apparent increase in temperature and related quantities (TVS, wattage) indicated in the time series data prior to the greatest ash-producing phase. In figures 17 and 18, volcanic signal begins to elevate no later than September 29, more than 24 hours before the reported initiation of the paroxysm on October 1. This follows three observations of relatively lower activity in the prior five days. If this pattern is representative of other eruptions, by monitoring these features volcanologists can be alerted as a volcano moves from quiescence to unrest. But more importantly, one can observe the progression from sustained intermediate levels of activity, to periods of lower activity, and to rapid but observable elevation in intensity that may precede a plinian phase. This ability to forecast what the volcano will do next will be a valuable tool for emergency response personnel.

Confidence in the satellite observations can be improved by correlating these with observations made using other data sources, including seismic data and field studies. However, as many of the volcanoes in the region remain uninstrumented and infrequently visited, satellite observations can provide critical information at this time.

Chapter 6: Conclusions

Satellite data from the AVHRR sensor is a valuable tool for monitoring volcanic activity, as seen in the application of the techniques developed by the Alaska Volcano Observatory to the 1994 eruption of Kliuchevskoi Volcano. The data is collected frequently and is available at little or no cost to researchers and other interested parties. AVHRR is capable of observing volcanic features including elevated surface temperatures and eruption clouds. Although data with higher spatial and temporal resolution would be desirable, AVHRR can provide general information about the state of unrest at a volcano, as well as indicate with more detail the progress of an eruption.

AVHRR data that has not been geometrically corrected are best suited for quantitative analysis of volcanic thermal anomalies, since the feature of interest is often much smaller than the sampled area. Resampling can mask the size and intensity of the anomaly through smearing and dilution of the thermal data at low scan angles, and exaggerate the size of the anomaly at high scan angles. Use of geometrically corrected data is recommended for initially locating volcanic thermal anomalies and tracking eruption clouds, but the disadvantages introduced by resampling hinder meaningful quantitative analysis.

The 1994 eruption of Kliuchevskoi Volcano became evident in AVHRR imagery on September 8 with the observation of a high temperature thermal anomaly. This observation coincides with seismic data that indicates a significant increase in the level of unrest occurred that day, as well as ground observations of lava fountaining and gas and ash bursts. Analysis of the thermal anomaly at Kliuchevskoi during the course of the

eruption revealed repeating patterns of increased and decreased activity, as measured by AVHRR data. Activity maxima occurred on September 15, 20, 24, and 29 - Oct 1. These maxima do not share data collection characteristics (such as high viewing angle) that would lead to artificially high values, and are likely due to fluctuations in the eruption processes at Kliuchevskoi. The eruption culminated with a paroxysmal phase that began on September 29 and ended on October 1, and featured a high temperature thermal anomaly and a dense eruption cloud which was carried for hundreds of km to the east.

The techniques in which the number of flagged pixels (saturated, threshold, SRPs) in an anomaly are counted provide means of qualitatively assessing the state of unrest at a volcano. Although band 3 is the best indicator of quiescence vs. unrest using AVHRR data, maximum temperature analysis should include band 4 as well in order to identify more subtle variation in eruptive activity.

The total volcanic signal (TVS) algorithms used here incorporate the area of the anomaly as well as the intensity of each pixel value in the anomaly, and provide the best indication of finer scale oscillations in eruptive activity when using AVHRR data. Temporal analysis of TVS clearly shows changes in the level of activity that may go unnoticed during more conventional analyses. TVS7 is the preferred version of the algorithm, as it captures anomalies that may be featured in one of only bands 3 and 4. A weakness of this method is that pixels at all scan angles are weighted equally despite their different sizes.

The total volcanic wattage technique of describing the state of volcanic unrest derives a value of the radiative energy flux in watts by incorporating the area and radiative temperature of each pixel. This approach holds promise because it attempts to give proportional influence to those pixels that are greatest in area when quantifying the thermal anomaly. The wattage analysis method is best suited for monitoring relative changes in the state of unrest, and needs further development to be better understood. But the coarse patterns in amplitude are real, and give valuable information about the state of unrest at the volcano.

This study shows the utility of several parameters derived from AVHRR data for monitoring the evolution of a volcano from quiescence to unrest to paroxysm to quiescence. By applying these methods to other eruptions for which there is archive data available, the validity of these analysis techniques can be further evaluated. Once fully evaluated, the empirical and statistical analyses can be automated and employed to monitor multiple sites as each is covered by AVHRR, and provide alerts of volcanic activity change that may have gone unnoticed otherwise.

References Cited

Alaska Volcano Observatory. 2000. WWW site: http://www.avo.alaska.edu.

Casadevall, Thomas J., and Thompson, Theodore B. 1995. World map of volcanoes and principal aeronautical features. U.S. Geological Survey Geophysical Investigations Series Map GP-1011.

Dean, K., Servilla, M., Roach, A., Foster, B., and Engle, K. 1998. Satellite monitoring of remote volcanoes improves study efforts in Alaska. Eos, Transactions, American Geophysical Union, Vol. 79, No. 35, September 1, 1998, 413, 422-423.

Global Volcanism Network Bulletin. 1994. v. 19 number 8.

Harris, A.J.L., Rothery, D.A., Carlton, S. Langaas, and Mannstein, H. 1995a. Non-zero saturation of the AVHRR thermal channels over high temperature targets: evidence from volcano data and a possible explanation. International Journal of Remote Sensing 16(1), 189-186.

Harris, A.J.L,. Swabey, S.E.J., and Higgins, J. 1995b. Automated thresholding of active lavas using AVHRR data. International Journal of Remote Sensing, 16(18), 3681-3686.

Hastings, David A., and Emery, William J., 1992. The Advanced Very High Resolution Radiometer (AVHRR): a Brief Reference Guide, in Photogrammetric Engineering and Remote Sensing, Vol. 58, No. 8, pp. 1183-1188.

Holasek, Rick E., and Rose, William I. 1991. Anatomy of 1986 Augustine volcano eruptions as recorded by multispectral image processing of digital AVHRR weather satellite data. Bulletin of Volcanology 53:420-435.

Hudson, Richard D. 1968. Infrared System Engineering. John Wiley and Sons, New York.

Kidwell, Katherine B., 1991. NOAA Polar Orbiter Data Users Guide, NOAA, Satellite Data Services Division, World Weather Building, Washington, DC.

Lillesand, Thomas M., and Kiefer, Ralph W. 1994. Remote Sensing and Image Interpretation, John Wiley and Sons, Inc.

Miller, T.P., McGimsey, R.G., Richter, D.H., Riehle, J.R., Nye, C.J., Yount, M.E., and Dumoulin, J.A. 1998. Catalog of the Historically Active Volcanoes of Alaska. USGS Open File Report 98-582.

Mouginis-Mark, Peter J., Garbeil, Harold, and Flament, Pierre. 1994. Effects of Viewing Geometry on AVHRR Observations of Volcanic Thermal Anomalies, Remote Sens. Environ. 48:51-60.

Neal, Christina A., Casadevall, Thomas J., Miller, Thomas P., Hendley, James W. III, Stauffer, Peter H. 1997. Volcanic ash – danger to aircraft in the north Pacific. U. S. Geological Survey Fact Sheet 030-97.

Prate, A. J. 1989. Observations of volcanic ash clouds in the 10-12 μm window using AVHRR/2 data. International Journal of Remote Sensing, v.10 (4), pp, 751-761.

Rao, P. Krishna, Holmes, Susan J., Anderson, Ralph K., Winston, Jay S., Lehr, and Paul E. 1990. Weather Satellites: Systems, Data, and Environmental Applications. American Meteorology Society, Boston.

Richter, Donald H., Rosenkrans, Danny S., and Steigerwald, Margaret J. 1995. Guide to the Volcanoes of the Western Wrangell Mountains, Alaska - Wrangell-St. Elias National Park and Preserve. U. S. Geological Survey Bulletin 2072.

Simkin, Tom, and Siebert, Lee., 1994. Volcanoes of the World, Geoscience Press, Tucson.

United States Geological Survey Volcano Hazards Program. 2000. WWW site: http://volcanoes.usgs.gov/Hazards/Effects/Ash+Aircraft.html.

VolcanoWorld. 2000. WWW site: http://volcano.und.nodak.edu/vw.html.

Waara, Anthony, Conzemius, Patty, and Carlson, Christine. 1996. Bound for Bezymianny web page. http://earthview.sdsu.edu/412b/byzy/bezy.html.

Wood, Charles A., and Kienle, Jürgen. 1990. Volcanoes of North America, Cambridge University Press.

Wooster, M.J., and Rothery, D.A. 1997. Thermal monitoring of Lascar Volcano, Chile, using infrared data from the along-track scanning radiometer: a 1992-1995 time series. Bulletin of Volcanology, 58:566-579.